Commun. Comput. Phys.
doi: 10.4208/cicp.OA-2016-0220

Vol. **xx**, No. x, pp. 1-30
xxx 201x

A Moving Mesh Finite Difference Method for Non-Monotone Solutions of Non-Equilibrium Equations in Porous Media

Hong Zhang*and Paul Andries Zegeling

Department of Mathematics, Utrecht University, P.O.Box 80.010, 3508TA Utrecht, The Netherlands.

Communicated by Tao Zhou

Received 25 November 2016; Accepted (in revised version) 28 February 2017

Abstract. An adaptive moving mesh finite difference method is presented to solve two types of equations with dynamic capillary pressure effect in porous media. One is the non-equilibrium Richards Equation and the other is the modified Buckley-Leverett equation. The governing equations are discretized with an adaptive moving mesh finite difference method in the space direction and an implicit-explicit method in the time direction. In order to obtain high quality meshes, an adaptive monitor function with directional control is applied to redistribute the mesh grid in every time step, then a diffusive mechanism is used to smooth the monitor function. The behaviors of the central difference flux, the standard local Lax-Friedrich flux and the local Lax-Friedrich flux with reconstruction are investigated by solving a 1D modified Buckley-Leverett equation. With the moving mesh technique, good mesh quality and high numerical accuracy are obtained. A collection of one-dimensional and two-dimensional numerical experiments is presented to demonstrate the accuracy and effectiveness of the proposed method.

AMS subject classifications: 35C07, 35Q35, 65M50, 74S20, 76S05

Key words: Relaxation non-equilibrium Richards equation, modified Buckley-Leverett equation, saturation overshoot, traveling wave analysis, moving mesh finite difference method.

1 Introduction

For the past several decades, since the observations of saturation overshoot and gravity driven fingers [1–4], there have been a great deal of experimental and theoretical studies on the mechanism and modeling of such phenomena. Stauffer [5], Hassanizadeh

*Corresponding author. *Email addresses:* H.Zhang4@uu.nl (H. Zhang), P.A.Zegeling@uu.nl (P. A. Zegeling)

 ©201x Global-Science Press

and Gray [6], Kalaydjian et al. [7] proposed a dynamic (non-equilibrium) relationship between capillary pressure and saturation to explain the occurrence of non-monotone saturation and capillary pressure when water is injected into initially dry sandy porous media. Eliassi and Glass investigated three additional forms referring to as a hypodiffusive form, a hyperbolic form and a mixed form in [8], they obtained saturation overshoot successfully by using the hypodiffusive form [9]. Nieber et al. [10], Chapwanya and Stockie [11] investigated the gravity-driven fingers by supplementing the Richards equation with the dynamic capillary pressure-saturation relationship, as well as including hysteretic effects. Their results demonstrate that the non-equilibrium Richards equation is capable of reproducing realistic fingers for a wide range of physically relevant parameters. Inspired by fingering instabilities in the flow of thin films, Cueto-Felgueroso and Juanes [12] put forward a phase field model using the idea of including the effect of a macroscopic interface in the mathematical description of unsaturated flow. Their model predictions agreed well with the lab measurements [4]. In the above mentioned references, most of models can be described as extensions to the Richards equation, besides, other approaches characterizing the saturation overshoot have also been investigated. Refs. [13,14] studied a generalized theory by introducing percolating and non-percolating fluid phases into a traditional mathematical model. DiCarlo et al. [15] developed a multiphase, fractional flow approach to describe the physics behind the displacement front that includes the viscosity of the gas. Refs. [16–18] simulated saturation overshoot by incorporating the dynamic capillary pressure with a traditional fractional flow equation. Their results suggest that the non-equilibrium fractional flow equation has the ability to model saturation overshoot.

Among the proposed theories, two models incorporating the dynamic capillary pressure relationship have attracted considerable interest in recent years. One is the relaxation non-equilibrium Richards equation (RNERE), and the other is the modified Buckley-Leverett equation (MBLE). Results on stability, traveling wave (TW) solutions, global existence, phase plane analysis and uniqueness of weak solutions are given in [19–24]. Numerical simulations [10, 11, 21, 25, 26] of the RNERE and the MBLE show that with appropriate parameters, both models will generate non-monotonic distribution of saturation, and the RNERE can become unstable in 2D when the flow profiles are sufficiently non-monotonic [20] which agree with the TW analysis and stability result.

In order to numerically solve these non-equilibrium equations, a variety of numerical methods have been developed in literature. Peszynska and Yi [27] proposed a cell-centered finite difference method and a locally conservative Eulerian-Lagrangian method, but they noticed that such methods may cause instabilities in convection-dominated cases and for large dynamic effects. A finite difference method which combined a minmod slope limiter based on the first order upwind and Richtmyer's schemes was used by van Duijn et al. [21]. The solutions obtained by this scheme agreed well with the TW results. Wang and Kao [28] extended the second and third order central schemes to capture the nonclassical solutions of the MBLE. Kao et al. [25] split the MBLE into a high-

order linear equation and a nonlinear convective equation, and then integrated the linear equation with a pseudo-spectral method and the nonlinear equation with a Godunov-type central-upwind scheme. The computed solutions demonstrate that the higher-order spatial reconstruction using fifth-order WENO5 scheme gives more accurate numerical solutions. Hong et al. [29] adopted a fourth-order central difference scheme to resolve the spatial resolution and a standard fourth-order Runge-Kutta scheme to march the resulting algebraic system in time, they observed high wave number oscillatory waves under certain parametric conditions. But later work by de Moraes et al. [30] shows that those oscillatory waves do not satisfy threshold for the existence of non-monotonic wave fronts [21]. Thus they suggested to use schemes with nonlinear numerical stability properties to capture the different shock waves, as well as rarefaction waves.

When capturing solutions of the two-phase flow models numerically, one has to deal with the difficulty related to the steep wave fronts or shocks. Thus, extremely dense meshes are required at the steep fronts or shocks in order to produce physically correct solutions. To overcome this difficulty, several adaptive methods have been developed in the past. Hu and Zegeling [31] used a moving mesh finite element method to discretize the RNERE in the space direction. With the moving mesh technique, high mesh quality and accurate numerical solutions are obtained successfully. Dong et al. [32] combined a mixed finite element method and a finite volume method to handle the nonlinearities of the governing equations efficiently. By adopting the moving mesh method, they obtained accurate numerical solutions with fewer computational resources. Refs. [17, 26] studied the MBLE with adaptive moving mesh finite difference methods, their results show that to achieve the same accuracy, the adaptive methods need around a factor of 4-10 fewer grid points than the uniform grid case.

Since the moving mesh methods greatly outperform the uniform mesh methods, the objective of the present work is to study the numerical solutions of the non-equilibrium equations using an adaptive moving mesh finite difference method. This method is based on an MMPDE approach [33] which works for a general spatial dimension, but we focus only in 1D and 2D in this paper. In order to distribute the mesh points reasonably, we adopt an adaptive monitor function with directional control [34] and a smoothing technique base on a diffusive mechanism [35].

The other parts of the paper are organized as follows. Section 2 introduces the one-phase RNERE and the two-phase MBLE. For verification of the numerical solutions, we also present a review of the TW analysis and the stability results. In Section 3 we will present the moving mesh strategy based on a quasi-Lagrangian approach and discretize the system with a finite difference method in the space direction and an IMEX method in the time direction. In Section 4, several one-dimensional and two-dimensional numerical experiments are carried out to demonstrate the effectiveness of the proposed scheme. Finally, Section 5 ends with conclusions and further comments.

2 Background

In this section, we derive the mathematical models describing the two-phase flow in a homogeneous porous media. For a more detailed derivation, we refer to [16,36].

Consider a homogeneous porous medium with a constant porosity ϕ and a constant intrinsic permeability K. One formulation of the traditional macroscopic theory starts from the fundamental balance laws of continuum mechanics for two phases (the wetting phase and the non-wetting phase) inside the porous medium. Denote the saturation of the wetting phase as u, then for a fully saturated porous medium, the saturation of the non-wetting phase is $1-u$. In a two-dimensional situation, the mass conservation equations for the two phases read

$$\frac{\partial(\phi\rho_w u)}{\partial t}+\nabla\cdot(\rho_w\vec{v}_w)=0, \tag{2.1}$$

$$\frac{\partial(\phi\rho_n(1-u))}{\partial t}+\nabla\cdot(\rho_n\vec{v}_n)=0, \tag{2.2}$$

where ρ_α and $\vec{v}_\alpha$,$\alpha=n,w$ denote the density and the volumetric velocity of each phase.

Let z be the vertical coordinate taken as positive upward, then Darcy's law reads

$$\begin{aligned}\vec{v}_\alpha&=-\frac{k_{r,\alpha}K}{\mu_\alpha}(\nabla p_\alpha+\rho_\alpha g\vec{e}_z),\\&=-\lambda_\alpha(\nabla p_\alpha+\rho_\alpha g\vec{e}_z),\quad \alpha=n,w,\end{aligned} \tag{2.3}$$

where g is the gravitational acceleration constant, $\vec{e}_z$ is the unit vector in the z direction, $k_{r\alpha}$, μ_α, p_α and λ_α are the relative permeability function, viscosity, pressure and mobility of phase α, respectively. Under non-equilibrium conditions, Stauffer [5], Hassanizadeh and Gray [6], Kalaydjian [7] proposed that the phases pressure difference p_n-p_w can be written as a function of the equilibrium capillary pressure minus the product of the saturation rate of the wetting phase with a dynamic capillary coefficient τ [Pa s]:

$$p_n-p_w=P_c(u)-\tau\frac{\partial u}{\partial t}, \tag{2.4}$$

where P_c modeling the capillary pressure - saturation relationship under an equilibrium condition, is a smooth and decreasing function of saturation u, and τ can be explained as a relaxation time. We refer to [37] for a review of experimental work on dynamic effects in the pressure-saturation relationship.

2.1 Basic equations

2.1.1 The RNERE

First, we consider a one phase flow model. When the density of the wetting phase (e.g. water) is much larger than that of the non-wetting phase (e.g. air), it is suggested [36] to

consider the case $\rho_n = 0$, $p_n = 0$ and $\vec{v}_n = [0,0]^T$ as a first approximation. Then the non-wetting phase vanishes from the problem and one is left only with the wetting phase. Assuming ρ_w is constant, combining the mass equation (2.1), Darcy's law (2.3) and the dynamic capillary pressure relationship (2.4) gives the RNERE

$$\begin{cases} \dfrac{\partial u}{\partial t} - \dfrac{\partial}{\partial z}\Big(\dfrac{1}{\phi}\lambda_w \rho_w g\Big) + \nabla \cdot \Big[\dfrac{1}{\phi}\lambda_w \nabla p\Big] = 0, \\ p = P_c(u) - \tau \dfrac{\partial u}{\partial t}. \end{cases} \tag{2.5}$$

Substituting the pressure equation into the saturation equation, we obtain

$$\frac{\partial(\phi u)}{\partial t} - \frac{\partial}{\partial z}(\lambda_w \rho_w g) + \nabla \cdot \Big[\lambda_w \nabla \Big(P_c(u) - \tau \frac{\partial u}{\partial t}\Big)\Big] = 0. \tag{2.6}$$

For a simplification of the notation we write (2.6) as

$$\frac{\partial u}{\partial t} + \frac{\partial}{\partial x}F(u) + \frac{\partial}{\partial z}G(u) + \nabla \cdot [D(u)\nabla u] - \tau \nabla \cdot \Big[H(u)\nabla \frac{\partial u}{\partial t}\Big] = 0, \tag{2.7}$$

where

$$F(u) = 0, \qquad G(u) = -\frac{1}{\phi}\lambda_w \rho_w g,$$
$$D(u) = \frac{1}{\phi}\lambda_w P_c'(u), \qquad H(u) = \frac{1}{\phi}\lambda_w.$$

2.1.2 The MBLE

When the two phases (e.g. water and oil) are incompressible, define the total velocity $\vec{v}_T = \vec{v}_n + \vec{v}_w = [v_T^x, v_T^z]^T$ and the fractional flow rate of the wetting phase $f_w = \frac{\lambda_w}{\lambda_w + \lambda_n}$, then the velocity of the wetting phase can be expressed by

$$v_w = f[v_T + \lambda_n(\nabla(p_n - p_w) - (\rho_w - \rho_n)g)]. \tag{2.8}$$

Substituting (2.8) into (2.1) and incorporating (2.4), we can get a two-phase MBLE as (2.7), with

$$F(u) = \frac{1}{\phi}f_w(u)v_T^x, \qquad G(u) = \frac{1}{\phi}f_w(u)[v_T^z - \lambda_n(u)(\rho_w - \rho_n)g],$$
$$D(u) = \frac{1}{\phi}\lambda_n(u)f_w(u)P_c'(u), \qquad H(u) = \frac{1}{\phi}\lambda_n(u)f_w(u).$$

2.2 Traveling wave analysis and non-monotonic solutions

In this section we apply the TW analysis to show the behavior of the wetting front for various values of τ for the RNERE and the MBLE. The analysis is performed in one-dimension instead of two-dimensions.

2.2.1 Traveling wave analysis of the RNERE

In the z-direction, the RNERE reads

$$\frac{\partial u}{\partial t}+\frac{\partial G(u)}{\partial z}+\frac{\partial}{\partial z}\Big[D(u)\frac{\partial u}{\partial z}\Big]-\tau\frac{\partial}{\partial z}\Big[H(u)\frac{\partial^2 u}{\partial z\partial t}\Big]=0. \tag{2.9}$$

Consider a TW solution connecting u_- and u_+ ($u_+>u_-$), by introducing the TW coordinate $\eta=z-st$ and substituting the TW solution $u(\eta)$ into (2.6) we obtain a third order ordinary differential equation (ODE)

$$\begin{cases} -su'+[G(u)]'+[D(u)u']'+s\tau[H(u)u'']'=0, \\ u(\pm\infty)=u_(\pm), \quad u_+>u_-\in[0,1], \\ u'(\pm\infty)=u''(\pm\infty)=0, \end{cases}$$

where prime denotes differentiation with respect to η, the boundary conditions of the ODE are obtained by the definition of TW solutions. Integrating this equation over $(-\infty,\eta)$ yields the second-order ODE:

$$\begin{cases} -s(u-u_-)+[G(u)-G(u_-)]+D(u)u'+s\tau H(u)u''=0, \\ u(\pm\infty)=u_\pm, \end{cases} \tag{2.10}$$

with s determined by the Rankine-Hugoniot condition

$$s=\frac{G(u_+)-G(u_-)}{u_+-u_-}.$$

Rewrite (2.10) as a first order system of ODEs

$$\begin{cases} u'=v, \\ v'=\dfrac{1}{s\tau H(u)}\big[s(u-u_-)-[G(u)-G(u_-)]-D(u)v\big]. \end{cases} \tag{2.11}$$

This system has two equilibria:

$$(u,v)=(u_+,0), \quad (u,v)=(u_-,0).$$

The Jacobian of (2.11) reads

$$A=\begin{bmatrix} 0 & 1 \\ \frac{s-G'(u)}{s\tau H(u)} & -\frac{D(u)}{s\tau H(u)} \end{bmatrix},$$

and has eigenvalues

$$\lambda_\pm=\frac{1}{2s\tau H(u)}\Big[-D(u)\pm\sqrt{(D(u))^2-4s\tau H(u)(G'(u)-s)}\Big]. \tag{2.12}$$

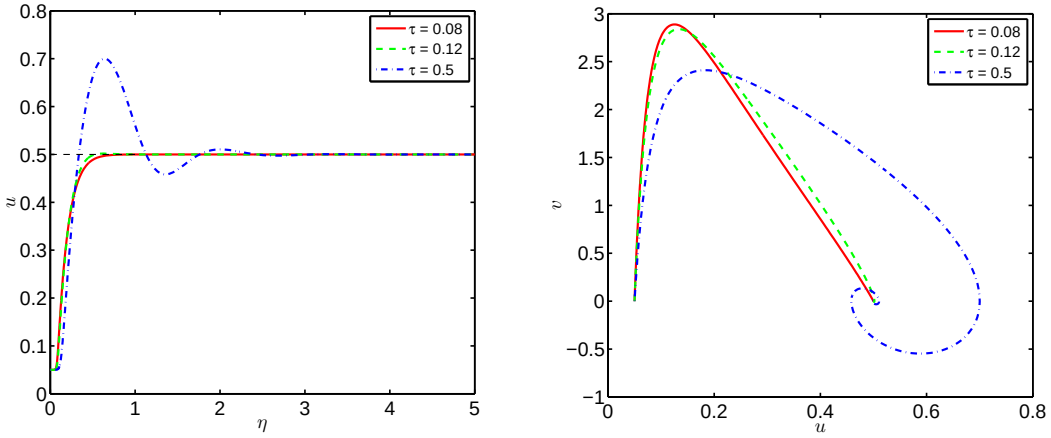

Figure 1: TW solutions (left) and phase plane plots (right) obtained with $\tau=0.08$, $\tau=0.12$, $\tau=0.5$.

For the RNERE (2.9), TW solutions are possible whenever $u_+ > u_-$. From (2.12) we can get the classification of the two equilibria. The equilibrium $(u_-,0)$ is a saddle and the equilibrium $(u_+,0)$ is either an unstable node or a spiral since $G'(u_+) > s$, where the critical value of the dynamic coefficient is defined as

$$\tau_s = \frac{D(u_+)^2}{4sH(u)(G'(u_+)-s)}. \tag{2.13}$$

When $\tau > \tau_s$, the equilibrium $(u_+,0)$ is a spiral, which means the saddle point $(u_-,0)$ is connected to the spiral point $(u_+,0)$. Fig. 1 depicts this situation in terms of the TW profiles (left) and phase plane plots (right) with the following choice of functions and parameters:

$$\begin{aligned} &G(u)=-u^\alpha, \quad D(u)=-\beta u^{\alpha-\beta-1}, \quad H(u)=u^\alpha, \quad \beta=0.25, \quad \alpha=3, \\ &u_+=0.5, \quad u_-=0.05. \end{aligned} \tag{2.14}$$

For this choice, (2.13) with u_+ gives $\tau_s=0.0843$. If $\tau<\tau_s$, the TW solution varies monotonically (red solid line). With the increment of $\tau>\tau_s$, the TW profile becomes more and more non-monotonic (green dashed and blue dash dotted lines).

2.2.2 The stability of the RNERE

The stability of the RNERE has been discussed in [19, 20, 38]. In a 2D situation, Ref. [19] pointed out that the wetting front for the RNERE is conditionally stable, i.e. stable for high frequency perturbations and unstable otherwise. In this section, we give a summary of the stability results presented in [20].

The stability analysis is based on imposing a small perturbation to the basic TW solution of (2.5). If the perturbation grows then the flow is unstable. In a 3D domain, the

perturbed TW solutions are described as the sum of the basic solutions and the perturbations:

$$u(x,y,\xi,t)=u_0(\xi)+\epsilon_0 e^{\mathrm{i}\omega_x x+\mathrm{i}\omega_y y+kt}u_1(\xi)+\mathcal{O}(\epsilon_0^2), \tag{2.15}$$

$$p(x,y,\xi,t)=p_0(\xi)+\epsilon_0 e^{\mathrm{i}\omega_x x+\mathrm{i}\omega_y y+kt}p_1(\xi)+\mathcal{O}(\epsilon_0^2), \tag{2.16}$$

where $u_0(\xi)$ and $p_0(\xi)$ are the basic traveling solutions of (2.5), ϵ_0 controls the magnitude of the perturbation, $\mathrm{i}=\sqrt{-1}$, $\omega=\omega_x^2+\omega_y^2$ is the wave number of the perturbation with ω_x and ω_y being the wave numbers in the x– and y–directions respectively. The functions $u_1(\xi)$ and $p_1(\xi)$ describe the variations of solutions and vanish at $\xi=\pm\infty$. The growth factor is denoted by k: if k is positive then the perturbation grows, otherwise it diminishes.

By substituting (2.15) into (2.5) and dropping the terms of order ϵ_0^2 and higher, the resulting perturbation equations are obtained for u_1 and p_1:

$$\begin{aligned}&\frac{\mathrm{d}A}{\mathrm{d}\xi}+\omega^2K(u_0)p_1=-ku_1,\\ &v\tau_0\frac{\mathrm{d}u_1}{\mathrm{d}\xi}+\left(P'(S_0)+v\frac{\partial\tau(u_0,p_0)}{\partial u}\frac{\mathrm{d}u_0}{\mathrm{d}\xi}\right)u_1+\left(v\frac{\tau(u_0,p_0)}{\partial p}\frac{\mathrm{d}u_0}{\mathrm{d}\xi}-1\right)p_1=-k\tau_0u_1,\end{aligned} \tag{2.17}$$

where A is the flux perturbation given by

$$A=-K(u_0)\frac{\mathrm{d}p_1}{\mathrm{d}\xi}-K'(u_0)\left(1+\frac{\mathrm{d}p_0}{\mathrm{d}\xi}u_1\right)+su_1,$$

and s is the velocity of the wetting front

$$s=\frac{K(u_+)-K(u_+)}{u_+-u_-}.$$

Nieber et al. [20] numerically solved the spectral problem (2.17) for various values of τ and ω. From Fig. 7 in [20], it is observed that when τ is small enough, the growth factor is negative for all wave numbers and therefore the saturation profile is stable. With increasing τ, the growth factor increases from negative to positive for wave numbers that are not too large. These results on the conditional stability of the RNERE show that the solution can be unstable if the parameters fall within a specified range.

In Section 2.2.3, we will investigate the stability of the RNERE by numerically solving (2.6) with perturbations and see whether we can observe a comparable behavior for the conditions under which perturbations can grow.

2.2.3 Computation of the growth factor of RNERE

In numerical simulations, for the purpose of examining the unstable behavior of the RNERE, we add a perturbation to the saturation field at $t=\frac{1}{2}T_{end}$ as

$$u=u_0+\epsilon_0\cos(\mathrm{i}\omega x)\frac{\partial u_0}{\partial z},$$

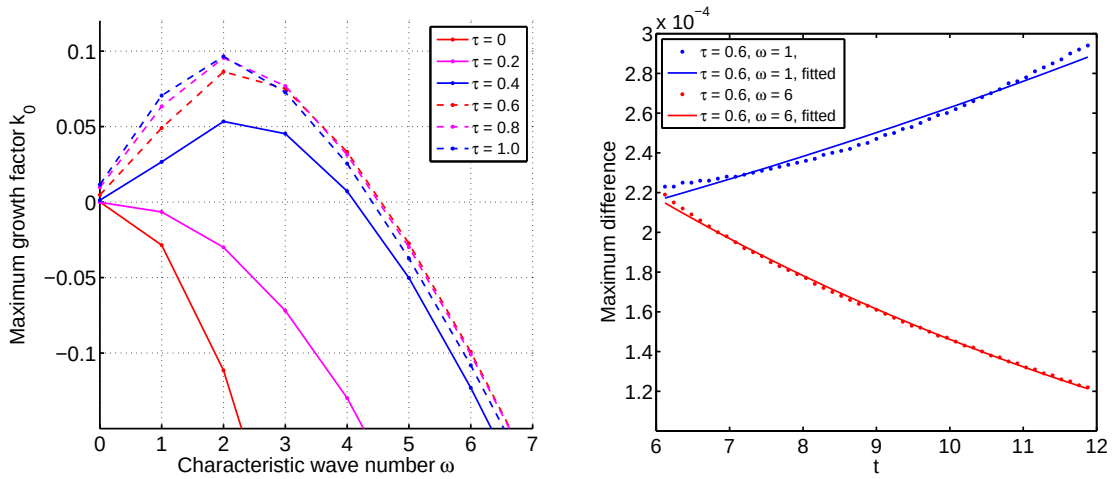

Figure 2: Growth factor vs. characteristic wave number for the RNERE for various values of τ (left); maximum difference between the perturbed and unperturbed saturation profiles and corresponding fitting curves as functions of time (blue: a growing perturbation with $\tau=0.6$, $\omega=1$, fitted curve $y=0.00016e^{0.0496t}$; red: a declining perturbation with $\tau=0.6$, $\omega=6$, fitted curve $y=0.00039e^{-0.0997t}$) (right).

where u_0 is the unperturbed solution computed at $\frac{1}{2}T_{end}$, ω is the wave number in the x-direction. The perturbation to the saturation is the product of a perturbation in the z-direction and a cosine shape perturbation in the x-direction.

In practice, for simplicity only integer values of ω are considered and the RNERE is solved in one period, which means for wave number ω_0, we set $\omega=1$ and solve the problem in the physical domain $[0,2\pi/\omega_0]\times[0,4]$. The first order derivative $\frac{\partial u_0}{\partial z}$ is approximated using the central difference scheme. By solving the RNERE with the perturbed saturation we can determine whether the amplitude of the perturbation increases or decreases in time. The RNERE (2.6) with functions and parameters (2.14) is solved from $t=0$ to $T_{end}=12$, first with the unperturbed saturation and then with the perturbed saturation. By subtracting the unperturbed saturation from the perturbed saturation we can get the maximum growth difference. The stability analysis in Section 2.2.2 shows that the evolution of the perturbation has an exponential change, thus we use an exponential least squares fit of the data points to determine the growth factor.

In Fig. 2 (left) we plot the computed relationship between the maximum growth factor k_0 and the wave number ω for different values of τ. It clearly shows similar behavior as the theoretical plot in Fig. 7 in [20]. When τ is small, the growth factor is negative for all wave numbers. With the increase of τ, the growth factor becomes positive for small wave numbers and the maximum growth factor increases as τ increases. In Fig. 2 (right) we plot the data points of the maximum growth difference together with the exponential fitting curves. We can see that the exponential function fits the maximum difference quite well.

2.3 Traveling wave analysis of the MBLE

The features of the MBLE are richer than the RNERE. In the two-phase situation, the flux function $G(u)=\frac{1}{\phi}f_w(u)[v_T^z+\lambda_n(u)(\rho_w-\rho_n)g]$ is usually a convex-concave function which introduces an additional difficulty to the TW analysis. This case has been extensively investigated in Refs. [21,23,39], where for a fixed value of u_-, the dependency between τ and the value u_+ is analyzed. For the MBLE the existence of the TW depends on τ. Here we consider $0<u_-<u_+<1$, and let u_I be the unique inflection point of the flux function $G(u)$, we summarize the results as obtained by [21]. For the details of the TW analysis, we refer to [21].

Similar to the TW analysis of the RNERE, the 1D MBLE in the z-direction also has the form (2.9) and can be transformed to the ODE (2.10). Consider the following options of $G(u)$, $D(u)$ and $H(u)$:

$$G(u)=\frac{u^2}{u^2+M(1-u)^2},\quad D(u)=-\epsilon,\quad H(u)=\epsilon, \tag{2.18}$$

then the results obtained by Ref. [21] can be summarized as follows.

When $u_0\in[0,u_I)$, it is proved that there is a constant τ_* such that for all $\tau\in[0,\tau_*]$, there exists a unique solution of (2.10) connecting $u_+=u_\alpha$ and $u_-=u_0$, where u_α is the unique root of the equation

$$G'(u)=\frac{G(u)-G(u_0)}{u-u_0}.$$

When $\tau>\tau_*$, there exists a unique constant $\bar{u}>u_\alpha$, such that (2.10) has a unique solution connecting $u_+=\bar{u}$ and $u_-=u_0$. For $u_-=u_0<u_+=u_B<\bar{u}(\tau)$, the solution of (2.10) will exist only if $u_B\in(u_0,\underline{u})$, where $\underline{u}$ is the unique root in the interval $(u_0,\bar{u})$ of

$$\frac{G(u)-G(u_0)}{u-u_0}=\frac{G(\bar{u})-G(u_0)}{\bar{u}-u_0}.$$

When $\tau>\tau_*$ and $u_B\in(\underline{u},\bar{u})$, there is no TW solution of (2.10) connecting $u_+=u_B$ and $u_-=u_0$. In this situation, the solution profile is non-monotonic, two TWs are used in succession: one from $u_+=u_B$ to $u_-=\bar{u}$ and one from $u_+=\bar{u}$ to $u_-=u_0$. For any $u_B\in(\underline{u},\bar{u})$ and $\tau>\tau_*$, there exists a unique solution of (2.10) such that $u_+=u_B$, $u_-=\bar{u}$.

For a given $\bar{u}>u_\alpha$, an algorithm to determine the value of τ is presented in Ref. [21]. This is based on the following concept, invert the function $u(\eta)$ and define the new dependent variable $w(u)=-u'(\eta(u))$, which satisfies

$$s\tau H(u)ww'-D(u)w=s(u-u_-)-[G(u)-G(u_-)],$$

with boundary condition

$$w(u_-=u_0)=w(u_+=\bar{u})=0.$$

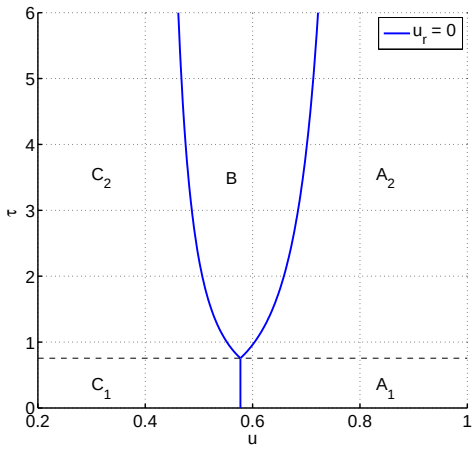

Figure 3: Bifurcation diagram for options (2.18) with $u_0=0$.

The value of τ corresponding to a given $\bar{u}$ can be computed using a shooting method proposed by [21]. To show the relationship between τ-$\bar{u}$, we take $M=0.5$, $\epsilon=10^{-3}$, and plot the bifurcation diagram for $u_0=0$ in Fig. 3.

When $u_0<u_I$ and $u_B>u_0$, the traveling solutions can be classified using the five regions in the bifurcation diagram. The results summarized from Ref. [21] are given in Table 1.

Table 1: TW results of the 1D MBLE (2.9) and (2.18) summarized from Ref. [21].

Region	Solution description
$(u_B,\tau)\in A_1$	Rarefaction wave from u_B down to u_α trailing an admissible Lax shock from u_α down to u_0
$(u_B,\tau)\in A_2$	Rarefaction wave from u_B down to $\bar{u}$ trailing an undercompressive shock from $\bar{u}$ down to u_0
$(u_B,\tau)\in B$	An admissible Lax shock from u_B up to $\bar{u}$ (may exhibit oscillations near $u_+=u_B$) trailing an undercompressive shock from $\bar{u}$ down to u_0
$(u_B,\tau)\in C_1$	An admissible Lax shock from u_B down to u_0
$(u_B,\tau)\in C_2$	An admissible Lax shock from u_B down to u_0 (may exhibit oscillations near $u_+=u_B$

3 An Adaptive moving mesh finite difference method

In this section, we describe the numerical procedure of the moving mesh FD method for solving the non-equilibrium equations. This method is based on the quasi-Lagrangian approach [40] in which we first transform the physical PDE from the physical coordinates

(x,z,t) to the computational coordinates (ξ,η,t) and then discretize it using an FD scheme in the space direction and an IMEX scheme in the time direction.

In the moving mesh situation, the uniform rectangular mesh is always redistributed as a non-rectangular mesh, thus introduces a difficulty to the FD discretization. In order to fix the problem we apply a coordinate transformation to (2.7). Let (x,z) and (ξ,η) denote the physical and computational coordinates. Without loss of generality, (x,z) is assumed to be in the interval $\Omega_p=[x_{\min},x_{\max}]\times[z_{\min},z_{\max}]$ and $(\xi,\eta)\in\Omega_c=[0,1]\times[0,1]$. A general coordinate transformation is given by

$$x=x(\xi,\eta,t),\quad z=z(\xi,\eta,t),\quad t\in[0,T],$$

with boundary condition

$$x(0,\eta,t)=x_{\min},\quad x(1,\eta,t)=x_{\max},\quad z(\xi,0,t)=z_{\min},\quad z(\xi,1,t)=z_{\max}. \tag{3.1}$$

Using the transformation formulas:

$$\begin{aligned}
&u_x=\frac{1}{J}[(uz_\eta)_\xi-(uz_\xi)_\eta],\\
&D(u)u_x=\frac{D(u)}{J}[(uz_\eta)_\xi-(uz_\xi)_\eta],\\
&(D(u)u_x)_x=\frac{1}{J}\left[\Big(\frac{D(u)}{J}(z_\eta^2u_\xi-z_\xi z_\eta u_\xi)\Big)_\xi+\Big(\frac{D(u)}{J}(z_\xi^2u_\eta-z_\xi z_\eta u_\xi)\Big)_\eta\right],
\end{aligned}$$

where $J=x_\xi z_\eta-x_\eta z_\xi$ is the Jacobian of the coordinate transformation, the physical PDE can be transformed to its Lagrangian form

$$\begin{aligned}
&u_t+\frac{1}{J}\big(\underbrace{z_\eta F(u)-x_\eta G(u)}_{\tilde F}\big)_\xi+\frac{1}{J}\big(\underbrace{x_\xi G(u)-y_\xi F(u)}_{\tilde G}\big)_\eta\\
&+\frac{1}{J}\left[\Big(\underbrace{\frac{D(u)}{J}(z_\eta^2u_\xi+x_\eta^2u_\xi-z_\xi z_\eta u_\eta-x_\xi x_\eta u_\eta)}_{R}\Big)_\xi+\Big(\underbrace{\frac{D(u)}{J}(z_\xi^2u_\eta+x_\xi^2u_\eta-z_\xi z_\eta u_\xi-x_\xi x_\eta u_\xi)_\eta}_{S}\Big)\right]\\
&-\frac{\tau}{J}\left[\Big(\underbrace{\frac{H(u)}{J}(z_\eta^2u_{t\xi}+x_\eta^2u_{t\xi}-z_\xi z_\eta u_{t\eta}-x_\xi x_\eta u_{t\eta})}_{P}\Big)_\xi\right.\\
&\left.-\Big(\underbrace{\frac{H(u)}{J}(z_\xi^2u_{t\eta}+x_\xi^2u_{t\eta}-z_\xi z_\eta u_{t\xi}-x_\xi x_\eta u_{t\xi})}_{Q}\Big)_\eta\right]=0,\quad(\xi,\eta)\in\Omega_c.
\end{aligned}$$

For convenience, the above equation is written in a simpler form:

$$u_t+\frac{1}{J}\tilde F(u)_\xi+\frac{1}{J}\tilde G(u)_\eta+\frac{1}{J}[R_\xi+S_\eta]-\frac{\tau}{J}[P_\xi+Q_\eta]=0. \tag{3.2}$$

3.1 The spatial discretization

We will solve (3.2) in the computational domain with a method of lines approach. The space discretization results in a large system of ODEs containing both stiff and nonstiff parts which is suitable to be integrated using an IMEX method. By treating the nonstiff advection terms $F(u)$ and $G(u)$ explicitly and the stiff terms R_ξ, S_η, P_ξ and Q_η implicitly, we can get a nonlinear system of equations. Since the stiff terms contain functions that depend on u: $D(u)$ and $H(u)$, hence we linearize the nonlinear terms by approximating them at t^n instead of at t^{n+2}. In this way we can fully exploit the advantages of the IEMX method. Let the space steps $\Delta\xi = 1/\mathrm{NX}$, $\Delta\eta = 1/\mathrm{NZ}$, the computational domain Ω_c can be partitioned into $\mathrm{NX}\times\mathrm{NZ}$ equal sized cells $[\xi_i,\xi_{i+1}]\times[\eta_j,\eta_{j+1}]$, $i = 0,1,\cdots,\mathrm{NX}-1, j = 0,1,\cdots,\mathrm{NZ}-1$. Let Δt denote the time step size, the discretization of (3.2) can be written as

$$\begin{aligned}\frac{u^{n+1}-u^n}{\Delta t}&+\frac{1}{J^n_{i,j}}\left[\frac{\bar{\tilde{F}}^n_{i+1/2,j}-\bar{\tilde{F}}^n_{i-1/2,j}}{\Delta\xi}\right]+\frac{1}{J^n_{i,j}}\left[\frac{\bar{\tilde{G}}^n_{i,j+1/2}-\bar{\tilde{G}}^n_{i,j-1/2}}{\Delta\eta}\right]\\&+\frac{1}{J^n_{i,j}}\left[\frac{R^{n+1}_{i+1/2,j}-R^{n+1}_{i-1/2,j}}{\Delta\xi}\right]+\frac{1}{J^n_{i,j}}\left[\frac{S^{n+1}_{i,j+1/2}-S^{n+1}_{i,j-1/2}}{\Delta\eta}\right]\\&-\frac{\tau}{J^n_{i,j}}\left[\frac{P^{n+1}_{i+1/2,j}-P^n_{i-1/2,j}}{\Delta\xi}\right]-\frac{\tau}{J^n_{i,j}}\left[\frac{Q^{n+1}_{i,j+1/2}-Q^{n+1}_{i,j-1/2}}{\Delta\eta}\right]=0,\end{aligned}\tag{3.3}$$

where the advection terms are discretized into conservation forms with $\bar{\tilde{F}}$ and $\bar{\tilde{G}}$ the numerical fluxes in ξ-, η-direction, respectively:

$$\bar{\tilde{F}}_{i+1/2,j}=\bar{\tilde{F}}(u^-_{i+1/2,j},u^+_{i+1/2,j}),\quad \bar{\tilde{G}}_{i,j+1/2}=\bar{\tilde{G}}(u^-_{i,j+1/2},u^+_{i,j+1/2}).$$

Ref. [41] pointed out that in general a solution containing nonclassical waves cannot be approximated by standard schemes which rely almost entirely on the idea of suppressing variation (e.g. monotone or total-variation-diminishing (TVD) / total-variation-bounded (TVB) schemes). Therefore, we employ the central difference scheme

$$\bar{\tilde{F}}(u^-_{i+1/2,j},u^+_{i+1/2,j})=\bar{\tilde{F}}(u_{i,j},u_{i+1,j})=\frac{1}{2}[\tilde{F}(u_{i,j})+\tilde{F}(u_{i+1,j})],\tag{3.4}$$

and the local Lax-Friedrichs scheme

$$\bar{\tilde{F}}(u^-_{i+1/2,j},u^+_{i+1/2,j})=\frac{1}{2}[\tilde{F}(u^-_{i+1/2,j})+\tilde{F}(u^+_{i+1/2,j})-\max|\tilde{F}_u|\cdot(u^+_{i+1/2,j}-u^-_{i+1/2,j})],$$

where the third term stabilizes the scheme by adding dissipation and the maximum is taken between $u^-_{i,j}$ and $u^+_{i,j}$. Two approaches are used to give the values of $u^-_{i,j}$ and $u^+_{i,j}$, one is the standard local Lax-Friedrichs flux (LLF):

$$u^-_{i+\frac{1}{2},j}=u_{i,j},\quad u^+_{i+\frac{1}{2},j}=u_{i+1,j},\tag{3.5}$$

the other adopts the local Lax-Friedrichs flux with reconstruction using a linear approximation in each cell (LLFR) [42]:

$$\begin{aligned} &u^-_{i+\frac{1}{2},j}=u_{i,j}+\frac{\Delta\xi}{2}s_{i,j},\quad u^+_{i+\frac{1}{2},j}=u_{i+1,j}-\frac{\Delta\xi}{2}s_{i+1,j},\\ &s_{i,j}=\big(\mathrm{sign}(s^-_{i,j})+\mathrm{sign}(s^+_{i,j})\big)\frac{\|s^-_{i,j}s^+_{i,j}\|}{\|s^-_{i,j}\|+\|s^+_{i,j}\|},\\ &s^-_{i,j}=\frac{u_{i,j}-u_{i-1,j}}{\Delta\xi},\quad s^+_{i,j}=\frac{u_{i+1,j}-u_{i,j}}{\Delta\xi}. \end{aligned} \tag{3.6}$$

The discretization for $\bar{\bar{G}}$ is similar to that of $\bar{\bar{F}}$. Then we apply the central difference scheme to the diffusion terms, the mixed derivative terms and the coordinate derivatives, for example:

$$\begin{aligned} R^{n+1}_{i+1/2,j}=&\frac{D(u^n_{i+1/2,j})}{J^n_{i+1/2,j}}\Bigg[\big((z_\eta|^n_{i+1/2,j})^2+(x_\eta|^n_{i+1/2,j})^2\big)\frac{u^{n+1}_{i+1,j}-u^{n+1}_{i,j}}{\Delta\xi}\\ &-\big(z_\xi|^n_{i+1,j}z_\eta|^n_{i+1,j}+z_\xi|^n_{i+1,j}z_\eta|^n_{i+1,j}\big)\frac{u^{n+1}_{i+1,j+1}-u^{n+1}_{i+1,j-1}}{2\Delta\eta}\Bigg],\\ P^{n+1/2}_{i+1/2,j}=&\frac{D(u^n_{i+1/2,j})}{J^n_{i+1/2,j}}\Bigg[\big((z_\eta|^n_{i+1/2,j})^2+(x_\eta|^n_{i+1/2,j})^2\big)\frac{(u^{n+1}_{i+1,j}-u^n_{i+1,j})-(u^{n+1}_{i,j}-u^n_{i,j})}{\Delta t\Delta\xi}\\ &-\big(z_\xi|^n_{i+1,j}z_\eta|^n_{i+1,j}+z_\xi|^n_{i+1,j}z_\eta|^n_{i+1,j}\big)\frac{(u^{n+1}_{i+1,j+1}-u^n_{i+1,j+1})-(u^{n+1}_{i+1,j-1}-u^n_{i+1,j-1})}{2\Delta t\Delta\eta}\Bigg], \end{aligned}$$

and

$$\begin{aligned} &x_\xi|_{i,j}=\frac{x_{i+1,j}-x_{i-1,j}}{2\Delta\xi}, && x_\eta|_{i,j}=\frac{x_{i,j+1}-x_{i,j-1}}{2\Delta\eta},\\ &x_\xi|_{i,j+\frac{1}{2}}=\frac{1}{2}[(x_\xi)_{i,j}+(x_\xi)_{i,j+1}], && x_\eta|_{i+\frac{1}{2},j}=\frac{1}{2}[(x_\eta)_{i,j}+(x_\eta)_{i+1,j}]. \end{aligned}$$

By making a discretization of the entire equation (3.3) in the way as we described above, and bringing the terms that should be approximated at time t^{n+1} to the left-hand side of the equation and the other terms to the right hand side, we arrive at the following system of equations,

$$A(\bar{u}^n)\bar{u}^{n+1}=b(\bar{u}^n).$$

In order to solve this large system of equations, we adopt an iterative method - the Bi-Conjugate Gradient Stabilized (Bi-CGSTAB) method [43] which is provided by the package LASPACK [44]. The implementation of the moving mesh FD method is also realized using LASPACK.

3.2 An MMPDE-based moving mesh strategy

In the situation of moving mesh methods, in order to achieve high accuracy, the mesh points may be redistributed in many ways according to the choices of the monitor function. A mesh equation is often solved simultaneously with the transformed PDE so as to generate the mesh positions in tandem with the solution, as the Moving Finite Element method of [45], the Moving mesh PDE (MMPDE) approach [33] and the parabolic Monge-Ampere approach of [46], etc. In [47], based on the numerical tests, the authors concluded that the MMPDE6 works best for Burgers' equation, thus we consider the MMPDE6 for the RNERE and the MBLE which are extended forms of Burgers-type, and use an adaptive monitor with directional control [34].

The MMPDE6 in 2D reads

$$\text{MMPDE6:}\quad \begin{cases} \bar{\nabla}\cdot\bar{\nabla}\dot{x}=-\dfrac{1}{\tau_x}\bar{\nabla}\cdot(\mathbf{M}\bar{\nabla}x), \\ \bar{\nabla}\cdot\bar{\nabla}\dot{z}=-\dfrac{1}{\tau_z}\bar{\nabla}\cdot(\mathbf{M}\bar{\nabla}z), \end{cases} \quad \mathbf{M}=\begin{bmatrix} M_1 & 0 \\ 0 & M_2 \end{bmatrix}, \tag{3.7}$$

subject to the boundary condition (3.1), where $\bar{\nabla}=[\partial/\partial\xi,\partial/\partial\eta]^T$ is the computational gradient, $\mathbf{M}$ is a diagonal matrix monitor function which controls the mesh concentration, τ_x and τ_z are artificial time parameters determining the time-scale over which a mesh converges to steady state. Ref. [33] shows that when solved exactly, the mapping given by (3.7) is well defined for all time. As a boundary condition, it is required that the grid points in the corners do not move. Moreover, the boundary grid points can only move along that boundary. In practice, we solve the one-dimensional version of (3.7): $\dot{x}_{\xi\xi}=-\frac{1}{\tau_x}(M_1x_\xi)_\xi$ for the horizontal boundaries and $\dot{z}_{\eta\eta}=-\frac{1}{\tau_z}(M_2z_\eta)_\eta$ for the vertical boundaries.

3.3 An adaptive monitor function with directional control

In the moving mesh method, the monitor function $\mathbf{M}$ is chosen to cluster mesh points at critical regions where more accuracy is needed, thereby reducing errors introduced by the numerical scheme. In this work, we consider an adaptive monitor function [34, 48]

$$M_i=(1-\kappa)\gamma_i(t)+\kappa\omega_i,\quad i=1,2, \tag{3.8}$$

with a time-dependent normalization for each spatial direction:

$$\gamma_i(t)=\int_0^1\int_0^1\omega_i\mathrm{d}\xi\mathrm{d}\eta.$$

The monitor matrix $\mathbf{M}$ prescribes the monitor values for all directions. If the diagonal elements are identical, for example:

$$\omega_i=(|\bar{\Delta}u|^2)^{\frac{1}{4}},\quad \bar{\Delta}=\frac{\partial^2}{\partial\xi^2}+\frac{\partial^2}{\partial\eta^2},$$

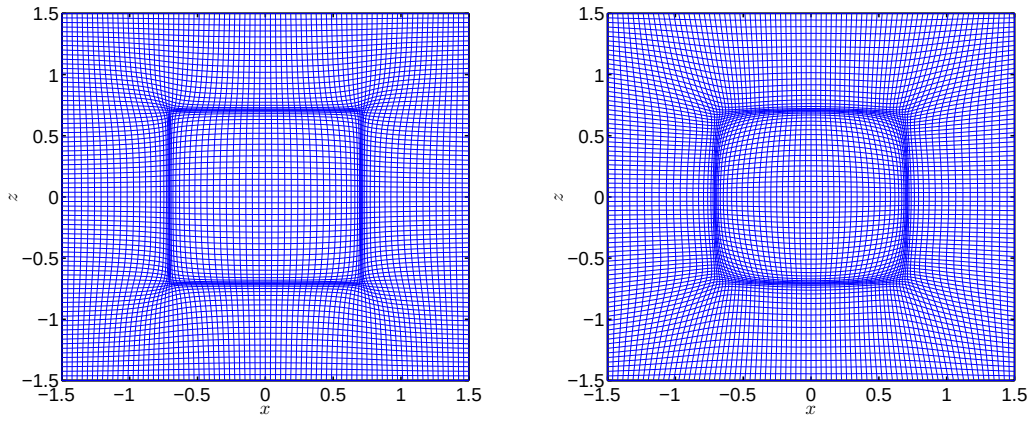

Figure 4: Initial meshes obtained by adaptive curvature type monitor with directional control (left) and without directional control (right) with parameters NX = NZ = 81, $\sigma = 2$, $\tau_x = \tau_z = 0.1$, $\kappa = 0.9$.

the mesh adaptation will be nondirectional (isotropic). Ref. [34] shows that a directional monitor function could produce much higher quality mesh at negligible costs, thus in this work we impose the directional control (anisotropic). The monitor components ω_i can be chosen as arc-length type in each direction

$$\omega_i = (|\bar{\nabla}_i u|^2)^{\frac{1}{2}}, \quad \bar{\nabla}_1 = \frac{\partial}{\partial \xi}, \ \bar{\nabla}_2 = \frac{\partial}{\partial \eta},$$

or curvature type

$$\omega_i = (|\bar{\Delta}_i u|^2)^{\frac{1}{4}}, \quad \bar{\Delta}_1 = \frac{\partial^2}{\partial \xi^2}, \ \bar{\Delta}_2 = \frac{\partial^2}{\partial \eta^2}.$$

In (3.8), the critical regions are identified by the derivatives computed with respect to the computational coordinates, which are smoother than the physical derivatives. The function $\gamma_i(t)$ averages the derivatives, resulting in an adaptive monitor function. The ratio of points in the critical regions is denoted by κ [49]. Thus the monitor matrix $\mathbf{M}$ is a symmetric positive definite matrix with different elements M_1 and M_2, therefore the mesh adaptivity becomes directional. In Fig. 4 we plot the adaptive meshes obtained using the adaptive curvature type monitor function with and without directional control for the initial condition (4.7) in Example 3-2. It shows that the monitor function with directional control can identify the critical regions more clearly than the one without directional control.

Since the computed monitor components M_i, $i = 1,2$ are usually non-smooth, in order to avoid a very distorted mesh around critical regions, in practice the components are generally smoothed [35, 50, 51] before the use for the integration of the MMPDE6. In our computation we apply a smoothing strategy based on a diffusive mechanism in [35]. Similar smoothing strategies have been adopted in [31, 32, 52] and obtained good results.

The smoothing equation in [35] is given by

$$\left[\mathcal{I}-\sigma_s(\sigma_s+1)\left((\Delta\xi)^2\frac{\partial^2}{\partial\xi^2}+(\Delta\eta)^2\frac{\partial^2}{\partial\eta^2}\right)\right]\tilde{M}_i=M_i,\quad i=1,2, \tag{3.9}$$

where $\mathcal{I}$ is the identity operator, σ_s is the spatial smoothing parameter. By solving (3.9) we can obtain a smoother monitor function $\tilde{\mathrm{M}}$ which introduces less singularity to (3.7), hence MMPDE6 can be solved more efficiently.

For solving the MMPDE we use the central difference discretization in the space direction and the Euler Backward integrator in the time direction. The monitor function **M** is calculated on beforehand, so that the system of equations resulting from the discretization is linear. This system is again solved using the Bi-CGSTAB method.

4 Numerical experiments

In this section we present numerical results obtained with the moving mesh FD method described in the previous section for a selection of examples. In all examples the time step used satisfies

$$\Delta t=\mathrm{C}\,\min_{i,j}\left(\frac{x_{i+1,j}-x_{i-1,j}}{2G'(u_{i,j})},\frac{z_{i,j+1}-z_{i,j}}{2F'(u_{i,j})}\right),$$

where C is called a CFL constant. To reduce the time integration error of the IMEX method, we use a CFL number of 0.2.

In the following subsections, the moving mesh FD method will be investigated with respect to both accuracy and efficiency.

4.1 Numerical convergence

In this section, numerical experiments will be carried out to demonstrate the effectiveness of the moving mesh FD method.

Example 1. In the first example, we will solve the 1D MBLE in z-direction with the central difference flux (3.4), the LLF flux (3.5) and the LLFR flux (3.6), then we decide which flux scheme is suitable for the computation of the MBLE. The accuracy and effectiveness of the moving mesh method are illustrated by comparing the numerical solutions obtained using the moving mesh with the solutions of the uniform mesh. This example is a 1D version of Example 5 with MBLE (2.11) and initial condition (4.5) in [25].

In (2.9) when $G(u)$, $D(u)$, $H(u)$ are given by

$$G(u)=\frac{u^2}{u^2+M(1-u)^2}(1-C(1-u)^2),\quad D(u)=-\epsilon,\quad H(u)=\epsilon^2,$$
$$M=0.5,\quad C=2,\quad \epsilon=10^{-3},\quad \tau=2.5,$$

with initial and boundary condition

$$u(z,0)=\begin{cases}0, & z\in[0,0.75],\\ 0.85, & z\in(0.75,2.25),\\ 0, & z\in[2.25,3],\end{cases} \tag{4.1}$$

$$u(0,t)=0,\quad u(3,t)=0,\quad t\in[0,0.48]. \tag{4.2}$$

By applying the shooting method proposed in [21] and using the traveling wave results, we can find that for the initial condition (4.1), a monotone basin of value $u\approx 0.3532$ exists in the drainage front together with a non-monotone plateau of value $u\approx 0.9449$ in the imbibition front. In Fig. 5, we plot the numerical solutions obtained by both uniform and moving mesh methods with different fluxes and monitors. In the top left figure one can see that when a uniform mesh with 2001^2 points is used, the central flux gives a higher plateau and a lower basin, the LLF flux results in no plateau and no basin while

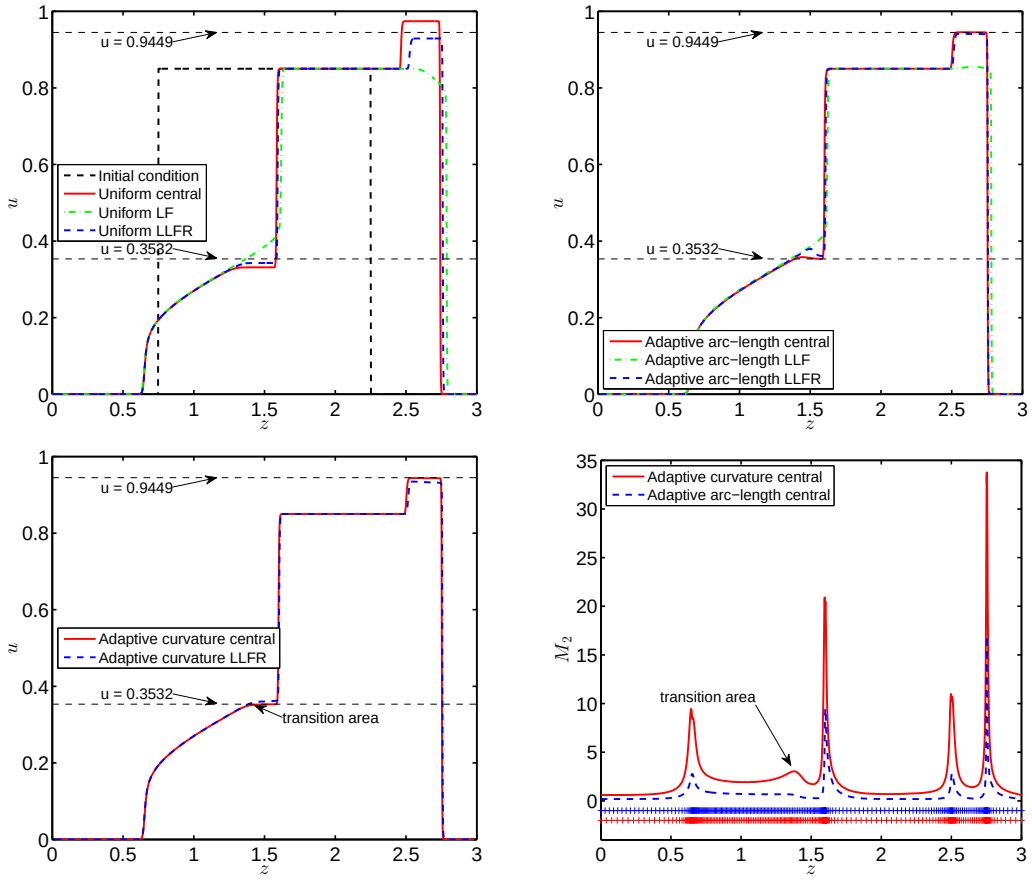

Figure 5: Solutions computed using the uniform mesh (NZ$=2001$, top left) and the moving mesh (NZ$=251$, $\sigma=2$, $\tau_z=0.1$, $\kappa=0.9$, top right); solutions (bottom left) and monitors (bottom right) obtained by the moving mesh using the arc-length type monitor and the curvature type monitor.

the LLFR flux obtains the closest plateau and basin values. These different results are deemed to be caused by the oscillation of the central flux, the diffusion of the LLF flux and the less diffusion of the LLFR flux. The top right figure shows that the when the moving mesh method with the arc-length type monitor function is used, the solutions obtained by all three fluxes get improved to some extent: the central flux gives the most accurate plateau and basin values, the LLFR flux gives better plateau value but there is oscillation near the basin area, the solution of the LLF flux gets a little improved but the plateau and basin values are still not acceptable because of the large diffusion of the flux. Although the central flux and the LLFR flux can give very accurate plateau and basin values, near the basin regions oscillations still appear because of a lack of grid points. Therefore, in the bottom left figure we show the results computed using the curvature type monitor function. It can be seen that when the transition areas near the basin regions are identified by the curvature type monitor (see the bottom right figure), the oscillations are removed, thus the basin profiles of central flux and LLFR flux get improved. From the above observations, it can be concluded that when the moving mesh method is used, the curvature type monitor with central flux can give the most accurate plateau and basin values, while in uniform mesh situation the LLFR flux gives closest plateau and basin values among the three fluxes.

Fig. 6 shows the convergence of both the uniform method with an increasing number of spatial grid points and the moving mesh method with an increasing of adaptivity parameter κ. As we can see from the figures, the finer is the uniform mesh, the more accurate solution we get, this obviously shows the numerical convergence of the FD method on uniform meshes. In the moving mesh case, when the adaptivity parameter κ becomes larger, more mesh points are clustered at critical regions, which gives plateau and basin heights with more accuracy. It is worth saying that for this example the moving mesh

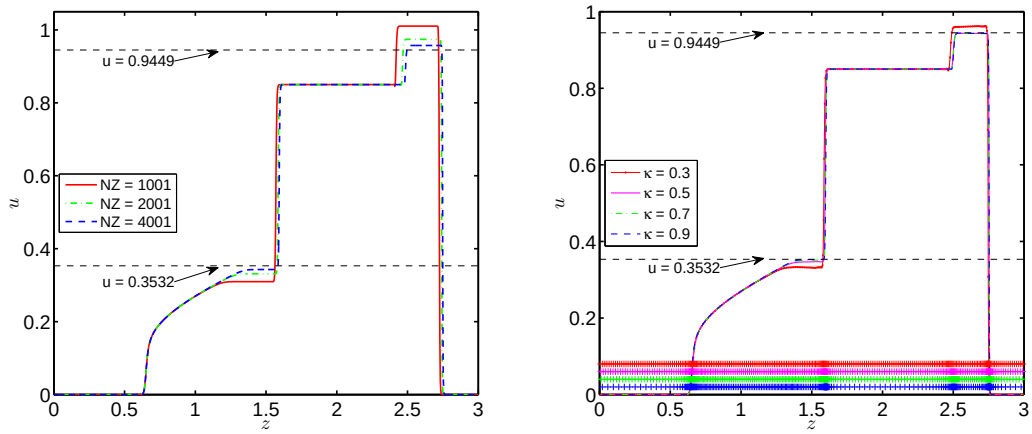

Figure 6: Example 1: solutions computed at $t=0.48$ using the uniform mesh (left figure: NZ$=$1001,2001,4001, central flux) and the moving mesh (right figure: NZ$=251$, $\sigma=2$, $\tau_z=0.1$, $\kappa=0.3$,0.5,0.7,0.9, central flux, curvature type monitor).

Table 2: Comparison of the CPU time [s] between the uniform mesh and the moving mesh case.

Uniform mesh		Moving mesh	
Mesh size	CPU time [s]	Adaptivity	CPU time [s]
1001	9.02	$\kappa=0.3$	9.72
2001	36.93	$\kappa=0.5$	16.98
4001	164.25	$\kappa=0.7$	25.91
-	-	$\kappa=0.9$	39.48

method needs approximately a factor of about 10 fewer grid points than the uniform mesh method to get the same plateau and basin values. The moving mesh method with 251 points and adaptivity $\kappa=0.9$ performs even better than the uniform mesh with 4001 points. Table 2 gives a comparison of CPU time between the uniform mesh cases and the moving mesh cases. As we can see, the CPU time increases with increasing mesh size and κ. The moving mesh of 251 points with $\kappa=0.3$ and $\kappa=0.9$ take almost the same time as the uniform mesh with 1001 and 2001 points, respectively, but the moving mesh solutions are more accurate than the uniform mesh solutions.

In Fig. 7 we plot the trajectories of the meshes obtained using different smoothing parameters. When there is non spatial smoothing, the grid trajectories oscillate in the space direction, as the smoothing parameters increase, the grid trajectories become smoother.

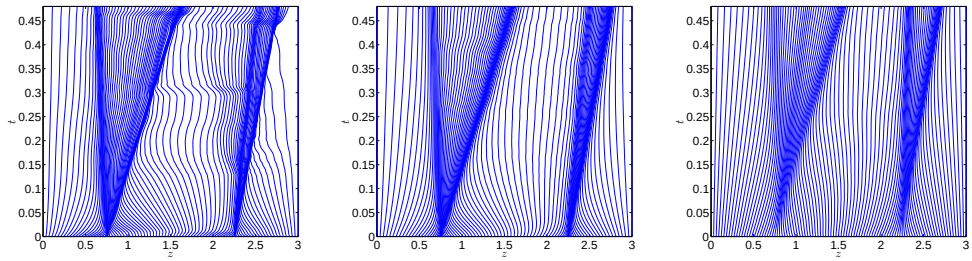

Figure 7: Grid (101 points) trajectories without spatial smoothing (left: $\sigma_s=0$, $\tau_s=0.1$); a grid with smoothing in both space and time variables (middle: $\sigma=2$, $\tau_s=0.1$) and a grid with too much smoothing (right: $\sigma_s=2$, $\tau_s=1$).

Example 2. Consider the 1D RNERE (2.9) with functions (2.14) and initial and boundary conditions

$$\begin{cases} u(z,t=0)=\dfrac{1}{2}(u_+-u_-)\left[1+\tanh\left(\dfrac{100(z-0.9(z_{\max}-z_{\min}))}{z_{\max}-z_{\min}}\right)\right]+u_-, \\ u(z=0,t)=u^-, \quad u(z=4,t)=u^+, \end{cases} \qquad z\in[0,4].$$

Fig. 8 presents the initial condition together with the solutions profiles and phase planes computed using the uniform mesh and moving mesh at time $t=12$. We choose NZ=101,401 for the uniform mesh and NZ=51,201 for the moving mesh. It shows that in

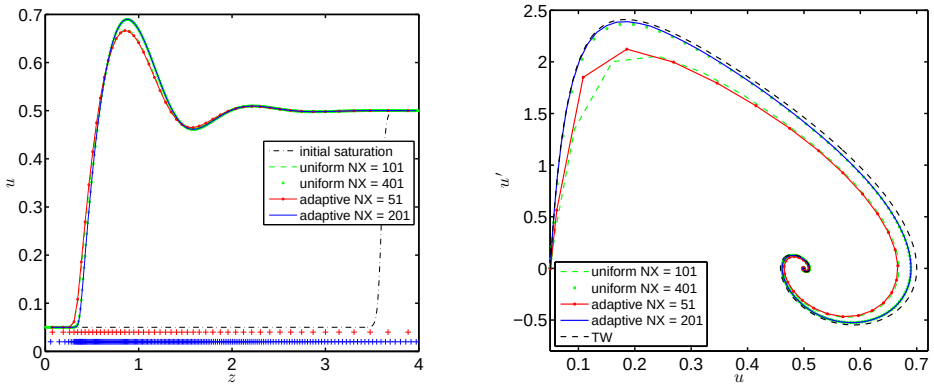

Figure 8: Example 2: solutions (left) and phase planes (right) computed at $t=12$ using the moving mesh (NZ=51,201, $\sigma=2$, $\tau_z=0.1$, $\kappa=0.9$) and uniform mesh (NZ=101,401).

the moving mesh situation, the mesh points are clustered near the critical regions, which helps to improve the accuracy of the solutions. The plots of the phase planes in Fig. 8 (right) also show that when the meshes are refined, both the uniform and moving mesh profiles converge to the TW result. It is worth saying that with the moving mesh method, the solutions computed using NZ = 201 points is comparable with the uniform mesh solution using 401 points. When NZ = 200, the moving mesh solution almost coincides with the TW solution.

4.2 Numerical experiments in 2D

Example 3-1. The first 2D problem is concerned with the MBLE (2.7) without dynamic capillary pressure and the functions are given by

$$\begin{cases} F(u)=\dfrac{u^2}{u^2+(1-u)^2}, \\ G(u)=f(u)(1-5(1-u)^2), \\ D(u)=-0.01, \quad H(u)=0.01^2, \end{cases} \tag{4.3}$$

the initial data is

$$u(x,z,0)=\begin{cases} 1, & x^2+z^2<0.5, \\ 0, & \text{otherwise}, \end{cases}$$

considered in the square domain $[-1.5,1.5]\times[-1.5,1.5]$.

This example is taken from [53] and has no exact solution. Zhang and Tang [42] solved this equation with an adaptive moving mesh finite volume method. Their results shows that the adaptive mesh solutions are more accurate than the uniform mesh ones. Since Example 1 demonstrates that the LLF flux is too diffusive, in Fig. 9 we only present the moving mesh solutions obtained by the central flux and the LLFR flux on different

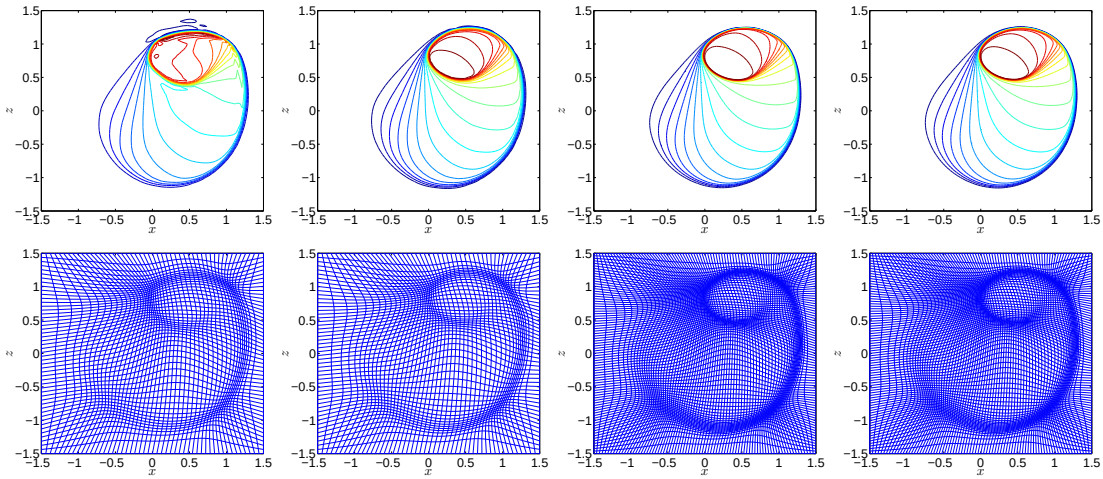

Figure 9: Example 3-1 with $\tau=0$: adaptive mesh solutions (top, $\sigma=2$, $\tau_x=\tau_z=0.1$, $\kappa=0.9$) and corresponding meshes (bottom) at $t=0.5$. From left to right: central flux 51^2 points, LLFR flux 51^2 points, central flux 81^2 points, LLFR flux 81^2 points.

meshes using the curvature type monitor. It is observed that on a mesh with 51^2 points, the central flux will cause oscillations near the upper front, while the LLFR flux gives smoother profiles. However, if we increase the mesh size to 81^2, there is no oscillation in the central flux solution and the solution is very close to the LLFR solution. By comparing Fig. 9 with the results presented in Ref. [42] in the eyeball norm, we may draw the conclusion that the moving mesh FD method performs as good as the moving mesh finite volume method.

Example 3-2. Next, we study two different initial conditions of the 2D MBLE with the dynamic capillary pressure term. The functions $F(u)$, $G(u)$, $D(u)$, $H(u)$ are the same as those used in Example 3-1. When dynamic coefficient τ is not zero, we can use the TW analysis in Section 2.3 to predict the behavior of the solution. Choosing $\tau=0.5$ and consider the 1D MBLE in the z direction, if the initial condition is taken as

$$u(z,0)=\begin{cases}0.9, & |z|<\sqrt{0.5},\\ 0, & \text{otherwise},\end{cases} \qquad z\in[-1.5,1.5], \tag{4.4}$$

the TW analysis shows that in the z direction, a saturation plateau of height $u\approx 0.97$ will appear at the shock front (see Fig. 10 left). For the 1D MBLE in the x direction, taking the initial condition as

$$u(x,0)=\begin{cases}0.9, & |x|<\sqrt{0.5},\\ 0, & \text{otherwise},\end{cases} \qquad x\in[-1.5,1.5], \tag{4.5}$$

the TW analysis shows that τ is too small to produce saturation overshoot, only monotone solution exists in the x-direction (see Fig. 10 right).

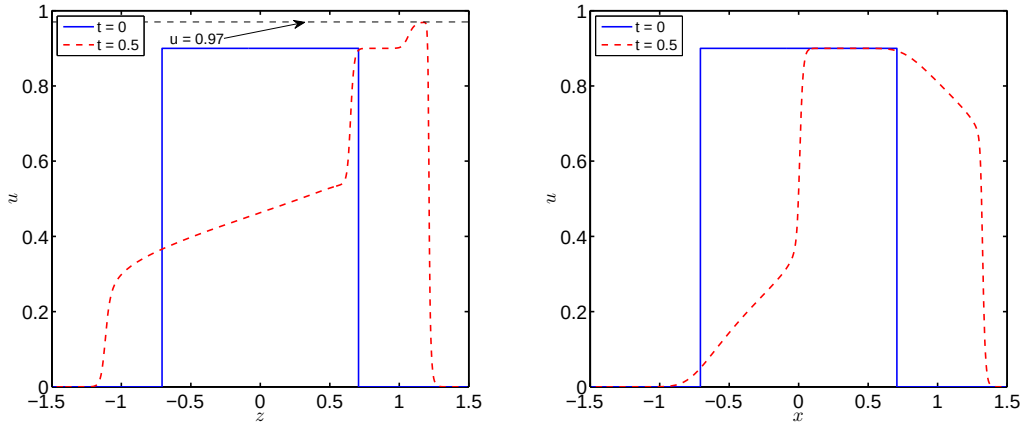

Figure 10: 1D MBLE with initial condition (4.4) (left) and (4.5) (right) at $t=0.5$.

Now, we study two different initial conditions: one with a cylindrical shape

$$u(x,z,0)=\begin{cases}0.9, & x^2+z^2<0.5,\\ 0, & \text{otherwise},\end{cases}\quad (x,z)\in[-1.5,1.5]\times[-1.5,1.5], \tag{4.6}$$

and one with a cubic shape

$$u(x,z,0)=\begin{cases}0.9, & x^2<0.5, z^2<0.5,\\ 0, & \text{otherwise},\end{cases}\quad (x,z)\in[-1.5,1.5]\times[-1.5,1.5]. \tag{4.7}$$

The solutions of the MBLE with initial condition (4.6) computed using the uniform mesh and the moving mesh are illustrated in Fig. 11. As one can see from Fig. 11, the MBLE generates a clear plateau at the shock front in the z-direction as expected. The plateau heights obtained by central flux are generally higher than those obtained by LLFR flux. The plateau height obtained by the moving mesh (301^2 points) with central flux is very close to the TW results, and is even more accurate than the plateau heights getting by the uniform mesh with 1001^2 points. This indicates about 10 times saving in the spatial grids, which is especially useful when dealing with 3D computations.

Since the LLFR flux performs better than the central flux in the uniform mesh situation, and the central flux performs better than the LLFR flux in the moving mesh situation, thus in Fig. 12 we show the results with initial condition (4.7) for the above choices. Similarly to the previous case of the initial condition (4.6), the non-monotone plateaus are located near the shock front in the z-direction and become thinner and lower along the positive x-direction because of the rarefaction waves created by the flux $F(u)$. Again, the moving mesh method gets a more accurate plateau height than the uniform mesh method.

Example 4. In the last example we simulate the finger phenomenon using the RNERE with the Brooks-Corey model. Ref. [54] presented snapshots of the finger phenomenon

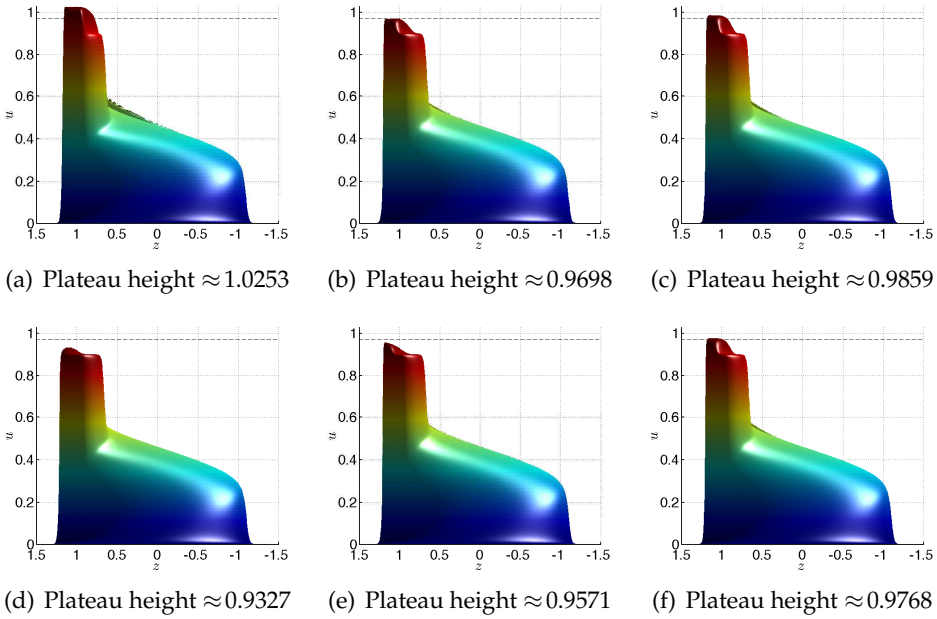

(a) Plateau height ≈1.0253 (b) Plateau height ≈0.9698 (c) Plateau height ≈0.9859

(d) Plateau height ≈0.9327 (e) Plateau height ≈0.9571 (f) Plateau height ≈0.9768

Figure 11: Example 3-2 with initial condition (4.6) at $t=0.5$: solutions obtained by the uniform mesh and adaptive mesh. Dashed line: $u=0.97$. Top row: central flux; bottom row: LLFR flux. Left column: uniform mesh 301^2 points; middle column: moving mesh 301^2 points ($\sigma=2$, $\tau_x=\tau_z=1$, $\kappa=0.6$); right column: uniform mesh 1001^2 points.

for water infiltrating into 20/30 sand. In this example, we use the RNERE (2.6) and the Brooks-Corey model to generate a single finger numerically. The physical parameters of the 20/30 sand [4,55] as well as the constants and the Brooks-Corey model [56] are listed in Table 3 and Table 4.

Table 3: Physical parameters for 20/30 sand.

			Drainage			Imbibition		
Sand	κ [m s^{-1}]	ϕ [-]	u_{re} [-]	λ [-]	p_d [Pa]	u_{re} [-]	λ [-]	p_d [Pa]
20/30	2.5×10^{-3}	0.35	0	5.57	850	0	5	490

Consider the physical domain $[0,0.3]\times[0,0.35]$[m], let $u_-=0.03$ and $u_+=0.4210$, we take the initial condition as

$$u(x,z,0)=u_-+\frac{1}{8}(u_+-u_-)\Big[\Big(1.0-\tanh(\frac{200}{x_{\max}-x_{\min}}(x-0.18))\Big)\times\Big(1.0+\tanh(\frac{200}{x_{\max}-x_{\min}}(x-0.12))\Big)\times\Big(1.0+\tanh(\frac{200}{z_{\max}-z_{\min}}(z-0.95(z_{\max}-z_{\min})))\Big)\Big].$$

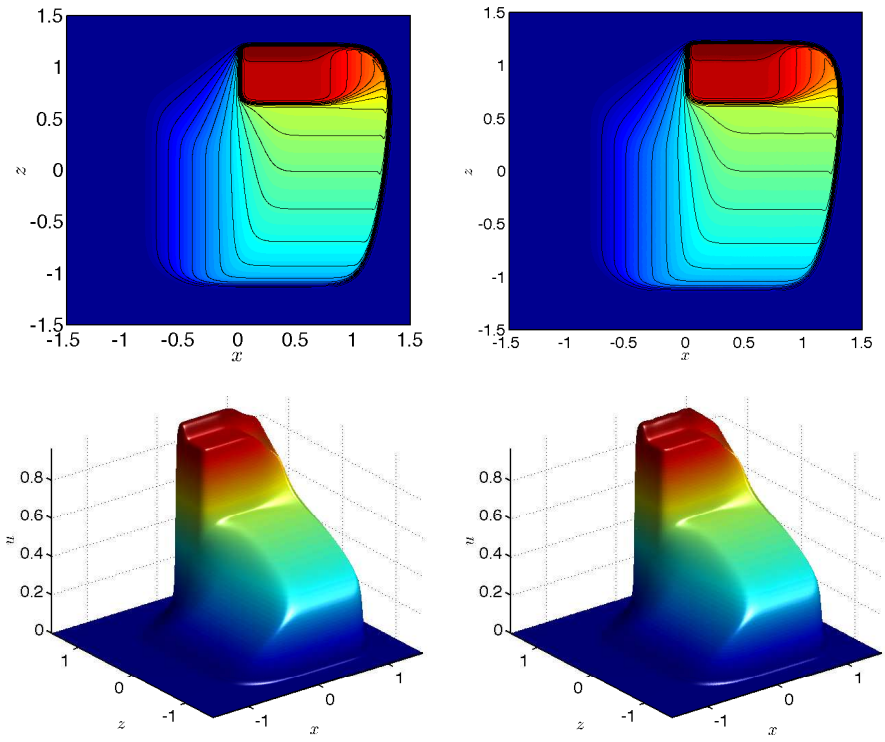

(a) Plateau height ≈ 0.9670 (b) Plateau height ≈ 0.9695

Figure 12: Example 3-2 with initial condition (4.7) at $t=0.5$: solutions obtained by the uniform mesh and the adaptive mesh. Left column: top and 3D views on uniform mesh (1001^2 points) with LLFR flux; right column: top and 3D views on moving mesh (301^2 points, $\sigma=2$, $\tau_x=\tau_z=1$, $\kappa=0.6$) with central flux.

Table 4: Constants and the Brooks-Corey model.

Density [kg m^{-3}]	$\rho_w=998.21$	$\rho_n=1.2754$
Viscosity [kg m^{-1}s^{-1}]	$\mu_w=1.002\times10^{-3}$	$\mu_n=1.82\times10^{-5}$
Mobility [m s kg^{-1}]	$\lambda_w=\frac{Kk_{rw}}{\mu_w}$	$\lambda_n=\frac{Kk_{rn}}{\mu_n}$
Constants	$g=9.81$ [m s^{-2}]	$K=\frac{\kappa\mu_w}{\rho_w g}$ [m^2]
	Capillary pressure	Relative permeability
Brooks-Corey model	$u_e=\frac{u-u_{re}}{1-u_{re}}$ $p_c=p_d u_e^{-\frac{1}{\lambda}}$, for $p_c>p_d$	$k_{rw}=u_e^{\frac{2+3\lambda}{\lambda}}$ $k_{rn}=(1-u_e)^2(1-u_e^{\frac{2+\lambda}{\lambda}})$

The initial saturation is presented is Fig. 13 (a). In this simulation, we use a Dirichlet boundary condition on the upper boundary $z=0.35$, a Neumann boundary condition on the lower boundary $z=0$, and a periodic boundary condition on the vertical boundaries.

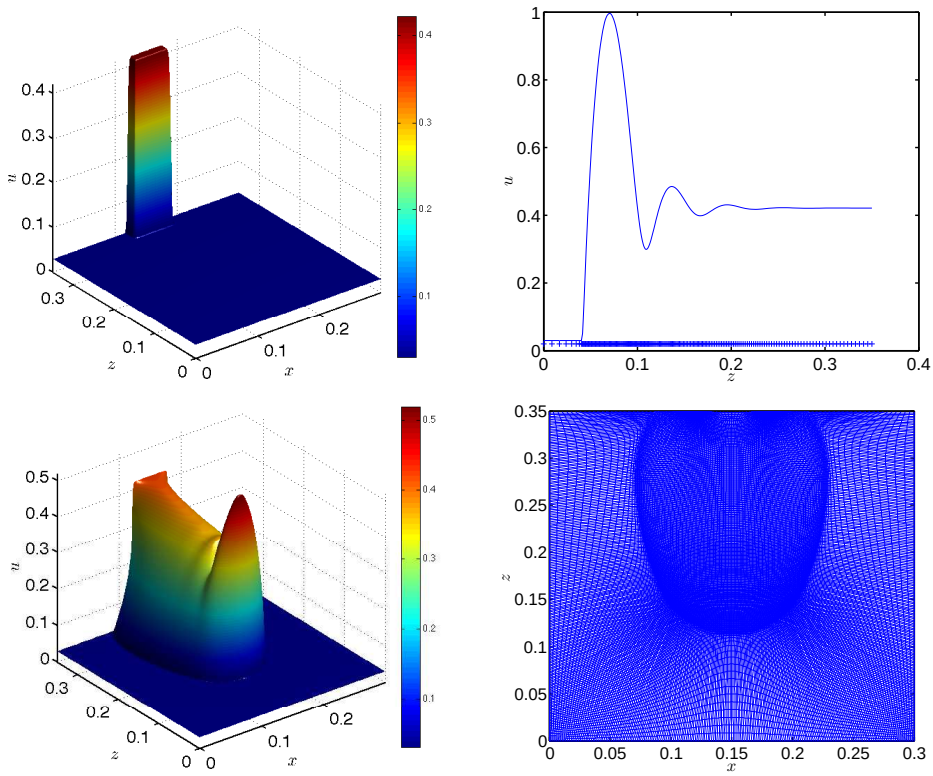

Figure 13: Example 4 at $t=350$, top left: 1D moving mesh solution with 201 points; top right: 2D initial saturation; bottom left: 2D moving mesh solution with 201^2 points; bottom right: 2D moving mesh with 201^2 points (right).

Fig. 13 (c,d) illustrate the results for the numerical simulation at $t=350$. Along the tail region, in contrast to the 1D simulation in Fig. 13 (b), the saturation profile for the 2D simulation decreases in the z-direction from the upper flow boundary and the overshoot saturation is lower than the value in 1D. This indicates that the lateral flow caused by the pressure gradient greatly influences the saturation profile. In real experiments, as is explained by [3], hysteresis is responsible for controlling the finger's sideways growth. In order to simulate realistic fingers, capillary pressure hysteresis has to be incorporated. Since our interest in this work is the dynamic capillary pressure effect, we would like to refer the interested readers to the discussions and simulations considering hysteresis in [10,11,57].

5 Conclusions

In the present work, we considered two types of non-equilibrium equations corresponding to the dynamic capillary pressure in porous media. We described the traveling waves for the relaxation non-equilibrium Richards equation and modified Buckley-Leverett equa-

tion, and the stability theory of the RNERE was verified by solving the governing equation numerically. Then we introduced a moving mesh finite difference method which is based on the quasi-Lagrangian formulation to approximate the RNERE and MBLE. The numerical scheme was tested on a suite of numerical experiments and showed to be robust. It enabled us to characterize the dynamic capillary effect in some 1D and 2D examples. In particular, we found that the moving mesh method performed much better than the uniform grid method and the central flux with adaptive curvature type monitor is more suitable for the simulating of flows in porous media.

Future work would extend the method of this paper to simulate the finger phenomenon incorporating both dynamic capillary pressure and capillary pressure hysteresis. This will improve the profile of the 2D finger by damping the lateral flow.

Acknowledgments

The research of H. Zhang was funded by the China Scholarship Council (No. 201503170430). We would like to thank the anonymous referees for their valuable comments and suggestions.

References

[1] D. Hill, J.-Y. Parlange, Wetting front instability in layered soils, Soil Science Society of America Journal 36 (5) (1972) 697–702.
[2] J. Selker, J.-Y. Parlange, T. Steenhuis, Fingered flow in two dimensions: 2. predicting finger moisture profile, Water Resources Research 28 (9) (1992) 2523–2528.
[3] R. J. Glass, T. S. Steenhuis, J.-Y. Parlange, Mechanism for finger persistence in homogeneous, unsaturated, porous media: Theory and verification., Soil Science 148 (1) (1989) 60–70.
[4] D. A. DiCarlo, Experimental measurements of saturation overshoot on infiltration, Water Resources Research 40 (4) (2004) W04215.
[5] F. Stauffer, Time dependence of the relations between capillary pressure, water content and conductivity during drainage of porous media, in: IAHR symposium on scale effects in porous media, Thessaloniki, Greece, Vol. 29, 1978, pp. 3–35.
[6] S. M. Hassanizadeh, W. G. Gray, Thermodynamic basis of capillary pressure in porous media, Water Resources Research 29 (10) (1993) 3389–3405.
[7] F.-M. Kalaydjian, et al., Dynamic capillary pressure curve for water/oil displacement in porous media: Theory vs. experiment, in: SPE Annual Technical Conference and Exhibition, Society of Petroleum Engineers, 1992.
[8] M. Eliassi, R. J. Glass, On the continuum-scale modeling of gravity-driven fingers in unsaturated porous media: The inadequacy of the Richards equation with standard monotonic constitutive relations and hysteretic equations of state, Water Resources Research 37 (8) (2001) 2019–2035.
[9] M. Eliassi, R. J. Glass, On the porous continuum-scale modeling of gravity-driven fingers in unsaturated materials: Numerical solution of a hypodiffusive governing equation that incorporates a hold-back-pile-up effect, Water resources research 39 (6) (2003) 1167.

[10] J. Nieber, A. Sheshukov, A. Egorov, R. Dautov, Non-equilibrium model for gravity-driven fingering in water repellent soils: Formulation and 2D simulations (2003) 245–258.
[11] M. Chapwanya, J. M. Stockie, Numerical simulations of gravity-driven fingering in unsaturated porous media using a nonequilibrium model, Water Resources Research 46 (9) (2010) W09534.
[12] L. Cueto-Felgueroso, R. Juanes, A phase field model of unsaturated flow, Water Resources Research 45 (10) (2009) W10409.
[13] R. Hilfer, F. Doster, P. Zegeling, Nonmonotone saturation profiles for hydrostatic equilibrium in homogeneous porous media, Vadose Zone Journal 11 (3) (2012). http://vzj.geoscienceworld.org/content/11/3/vzj2012.0021.
[14] F. Doster, P. Zegeling, R. Hilfer, Numerical solutions of a generalized theory for macroscopic capillarity, Physical Review E 81 (3) (2010) 036307.
[15] D. A. DiCarlo, M. Mirzaei, B. Aminzadeh, H. Dehghanpour, Fractional flow approach to saturation overshoot, Transport in porous media 91 (3) (2012) 955–971.
[16] C. van Duijn, S. Hassanizadeh, I. Pop, P. Zegeling, et al., Non-equilibrium models for two phase flow in porous media: the occurence of saturation overshoots, In: CAPM 2013 - Proceedings of the 5th International Conference on Applications of Porous Media (2013) 59–70.
[17] P. A. Zegeling, An adaptive grid method for a non-equilibrium PDE model from porous media, J. Math. Study 48 (2) (2015) 187–198.
[18] H. Zhang, P. A. Zegeling, A numerical study of two-phase flow models with dynamic capillary pressure and hysteresis, Transport in Prous media 116 (2) (2017) 825–846.
[19] A. G. Egorov, R. Z. Dautov, J. L. Nieber, A. Y. Sheshukov, Stability analysis of gravity-driven infiltrating flow, Water resources research 39 (9) (2003) 1266.
[20] J. L. Nieber, R. Z. Dautov, A. G. Egorov, A. Y. Sheshukov, Dynamic capillary pressure mechanism for instability in gravity-driven flows; review and extension to very dry conditions, Transport in porous media 58 (1-2) (2005) 147–172.
[21] C. Van Duijn, L. Peletier, I. Pop, A new class of entropy solutions of the Buckley-Leverett equation, SIAM Journal on Mathematical Analysis 39 (2) (2007) 507–536.
[22] A. Mikelić, A global existence result for the equations describing unsaturated flow in porous media with dynamic capillary pressure, Journal of Differential Equations 248 (6) (2010) 1561–1577.
[23] K. Spayd, M. Shearer, The Buckley-Leverett equation with dynamic capillary pressure, SIAM Journal on Applied Mathematics 71 (4) (2011) 1088–1108.
[24] X. Cao, I. Pop, Uniqueness of weak solutions for a pseudo-parabolic equation modeling two phase flow in porous media, Applied Mathematics Letters 46 (2015) 25–30.
[25] C.-Y. Kao, A. Kurganov, Z. Qu, Y. Wang, A fast explicit operator splitting method for modified Buckley-Leverett equations, Journal of Scientific Computing 64 (3) (2015) 837–857.
[26] H. Zhang, P. A. Zegeling, A numerical study of two-phase flow with dynamic capillary pressure using an adaptive moving mesh method, arXiv preprint arXiv:1604.04863.
[27] M. Peszynska, S.-Y. Yi, Numerical methods for unsaturated flow with dynamic capillary pressure in heterogeneous porous media, Int J Numer Anal Model 5 (Special Issue) (2008) 126–149.
[28] Y. Wang, C.-Y. Kao, Central schemes for the modified Buckley–Leverett equation, Journal of Computational Science 4 (1) (2013) 12–23.
[29] J. M.-K. Hong, J. Wu, J.-M. Yuan, The generalized Buckley-Leverett and the regularized Buckley-Leverett equations, Journal of Mathematical Physics 53 (5) (2012) 053701.
[30] G. de Moraes, R. d. S. Teixeira, L. S. d. B. Alves, Validity of parametric restrictions to the

modified Buckley-Leverett equations, Journal of Porous Media 19 (9) (2016) 811–819.
[31] G. Hu, P. A. Zegeling, Simulating finger phenomena in porous media with a moving finite element method, Journal of computational physics 230 (8) (2011) 3249–3263.
[32] H. Dong, Z. Qiao, S. Sun, T. Tang, Adaptive moving grid methods for two-phase flow in porous media, Journal of Computational and Applied Mathematics 265 (2014) 139–150.
[33] W. Huang, Y. Ren, R. D. Russell, Moving mesh partial differential equations (MMPDEs) based on the equidistribution principle, SIAM Journal on Numerical Analysis 31 (3) (1994) 709–730.
[34] A. Van Dam, P. Zegeling, Balanced monitoring of flow phenomena in moving mesh methods, Communications in Computational Physics 7 (1) (2010) 138–170.
[35] W. Huang, R. D. Russell, Analysis of moving mesh partial differential equations with spatial smoothing, SIAM Journal on Numerical Analysis 34 (3) (1997) 1106–1126.
[36] R. Hilfer, R. Steinle, Saturation overshoot and hysteresis for twophase flow in porous media, The European Physical Journal Special Topics 223 (11) (2014) 2323–2338.
[37] S. M. Hassanizadeh, M. A. Celia, H. K. Dahle, Dynamic effect in the capillary pressure–saturation relationship and its impacts on unsaturated flow, Vadose Zone Journal 1 (1) (2002) 38–57.
[38] A. Egorov, R. Dautov, J. Nieber, A. Sheshukov, Stability analysis of traveling wave solution for gravity-driven flow, Developments in Water Science 47 (2002) 121–128.
[39] C. Van Duijn, Y. Fan, L. Peletier, I. S. Pop, Travelling wave solutions for degenerate pseudo-parabolic equations modelling two-phase flow in porous media, Nonlinear Analysis: Real World Applications 14 (3) (2013) 1361–1383.
[40] H. Weizhang, R. D. Russell, Adaptive moving mesh methods, Vol. 174, Springer Science & Business Media, 2010.
[41] F. Kissling, C. Rohde, The computation of nonclassical shock waves in porous media with a heterogeneous multiscale method: the multidimensional case, Multiscale Modeling & Simulation 13 (4) (2015) 1507–1541.
[42] Z.-R. Zhang, T. Tang, An adaptive mesh redistribution algorithm for convection-dominated problems, Communications on Pure and Applied Analysis 1 (3) (2002) 341–357. doi:10.3934/cpaa.2002.1.341.
URL `http://aimsciences.org/journals/displayArticlesnew.jsp?paperID=116`
[43] H. A. Van der Vorst, Bi-cgstab: A fast and smoothly converging variant of Bi-CG for the solution of nonsymmetric linear systems, SIAM Journal on scientific and Statistical Computing 13 (2) (1992) 631–644.
[44] T. Skalicky, Laspack 1.12. 2 (1995),
URL http://dddas. org/mgnet/Codes/laspack/html/laspack. html.
[45] K. Miller, R. N. Miller, Moving finite elements. I, SIAM Journal on Numerical Analysis 18 (6) (1981) 1019–1032.
[46] C. J. Budd, J. Williams, Moving mesh generation using the parabolic Monge-Ampere equation, SIAM Journal on Scientific Computing 31 (5) (2009) 3438–3465.
[47] W. Huang, Y. Ren, R. D. Russell, Moving mesh methods based on moving mesh partial differential equations, Journal of Computational Physics 113 (2) (1994) 279–290.
[48] P. Zegeling, W. De Boer, H. Tang, Robust and efficient adaptive moving mesh solution of the 2-D Euler equations, Contemporary Mathematics 383 (2005) 419–430.
[49] W. Huang, Practical aspects of formulation and solution of moving mesh partial differential equations, Journal of Computational Physics 171 (2) (2001) 753–775.
[50] J. G. Verwer, J. Blom, R. Furzeland, P. Zegeling, A moving-grid method for one-dimensional

PDEs based on the method of lines, Stichting Mathematisch Centrum, 1988.
[51] G. Beckett, J. Mackenzie, A. Ramage, D. Sloan, On the numerical solution of one-dimensional PDEs using adaptive methods based on equidistribution, Journal of Computational Physics 167 (2) (2001) 372–392.
[52] H. Wang, R. Li, T. Tang, Efficient computation of dendritic growth with r-adaptive finite element methods, Journal of Computational Physics 227 (12) (2008) 5984–6000.
[53] K. H. Karlsen, K. Brusdal, H. K. Dahle, S. Evje, K.-A. Lie, The corrected operator splitting approach applied to a nonlinear advection-diffusion problem, Computer methods in applied mechanics and engineering 167 (3) (1998) 239–260.
[54] T. Bauters, D. DiCarlo, T. Steenhuis, J.-Y. Parlange, Soil water content dependent wetting front characteristics in sands, Journal of Hydrology 231 (2000) 244–254.
[55] M. Schroth, J. Istok, S. Ahearn, J. Selker, Characterization of miller-similar silica sands for laboratory hydrologic studies, Soil Science Society of America Journal 60 (5) (1996) 1331–1339.
[56] R. H. Brooks, A. Corey, Properties of porous media affecting fluid flow, Journal of the Irrigation and Drainage Division 92 (2) (1966) 61–90.
[57] G. Sander, O. Glidewell, J. Norbury, Dynamic capillary pressure, hysteresis and gravity-driven fingering in porous media, in: Journal of Physics: Conference Series, Vol. 138, IOP Publishing, 2008, p. 012023.